



## Article

# Estimating Fine Fuel Load Using Sentinel-2A Imagery and Machine Learning: A Case Study in the Mountainous Forests of Changsha, China

Lei Deng <sup>1,2,3</sup> , Enping Yan <sup>1,2,3</sup>, Jiawei Jiang <sup>4</sup> and Dengkui Mo <sup>1,2,3,\*</sup>

- <sup>1</sup> Research Center of Forestry Remote Sensing & Information Engineering, Central South University of Forestry & Technology, Changsha 410004, China; leideng@csuft.edu.cn (L.D.); enpingyan@csuft.edu.cn (E.Y.)
- <sup>2</sup> Hunan Provincial Key Laboratory of Forestry Remote Sensing Based Big Data & Ecological Security, Changsha 410004, China
- <sup>3</sup> Key Laboratory of National Forestry and Grassland Administration on Forest Resources Management and Monitoring in Southern China, Changsha 410004, China
- <sup>4</sup> School of Civil Engineering, Sun Yat-Sen University, Zhuhai 519082, China; jiangjw26@mail2.sysu.edu.cn
- \* Correspondence: dengkuimo@csuft.edu.cn

**Abstract:** Fine fuel load (FFL) is a crucial variable influencing the occurrence of wildfire. Accurate knowledge of the distribution of FFL in mountainous forests is essential for ongoing wildfire risk management and the stability of mountain ecosystems. Traditional methods of estimating forest fuel load typically involve ground surveys combined with remote sensing, which can be costly and inefficient. Therefore, low-cost, large-scale FFL estimation remains challenging. In this study, Sentinel-2A satellite imagery from the Changsha forest region was used as the data source. Firstly, different feature variables were constructed based on false-color (B843), true-color (B432), four-band (B8432) combinations, and the Normalized Difference Water Index (NDWI). Subsequently, a machine learning approach based on random convolution was employed to estimate FFL. This study also included accuracy assessments of the estimation results and the creation of FFL maps for the study area. The results showed that the FFL estimation based on the B8432 band combination achieved the highest accuracy, with RMSE and  $R^2$  values of  $5.847 \text{ t}\cdot\text{hm}^{-2}$  and 0.656, respectively. FFL estimation results based on false-color imagery followed, with true-color imagery and NDWI index-based estimation results exhibiting lower accuracy. This study offers critical FFL insights using random convolution techniques applied to Sentinel-2A imagery, enhancing the ability to monitor and manage forest fuel conditions effectively, thereby facilitating more informed regional wildfire risk management strategies.

**Keywords:** fine fuel load; wildfire; mountain ecosystem; Sentinel-2A; random convolution; machine learning



**Citation:** Deng, L.; Yan, E.; Jiang, J.; Mo, D. Estimating Fine Fuel Load Using Sentinel-2A Imagery and Machine Learning: A Case Study in the Mountainous Forests of Changsha, China. *Remote Sens.* **2023**, *15*, 5721. <https://doi.org/10.3390/rs15245721>

Academic Editors: Bogdan Andrei Mihai and Marcel Torok

Received: 18 October 2023

Revised: 7 December 2023

Accepted: 8 December 2023

Published: 14 December 2023



**Copyright:** © 2023 by the authors. Licensee MDPI, Basel, Switzerland. This article is an open access article distributed under the terms and conditions of the Creative Commons Attribution (CC BY) license (<https://creativecommons.org/licenses/by/4.0/>).

## 1. Introduction

Forest fires are intricately linked to human life, often resulting in negative impacts primarily in the form of natural resource losses and threats to human safety. Secondary damages include the destruction of homes and public buildings [1]. A key factor in the occurrence of forest fires is the presence of combustible materials within the forest. The interrelation between forest fuels and mountainous ecosystems is notably close-knit. Owing to the complexity of the terrain and diverse climatic conditions, fuel accumulation can happen rapidly. This accumulation heightens the risk of forest fires, which, in turn, can disrupt the balance of mountainous ecosystems. Therefore, controlling forest fuels is essential for the maintenance and protection of these ecosystems. Managing forest fuels effectively not only reduces the likelihood of wildfires but also helps in preserving the ecological integrity and biodiversity of these critical habitats. Combustible materials

in forests can be categorized into multiple types based on their sources and physical properties [2]. Any category of combustible material can potentially ignite, leading to forest fires. The level of combustible material, known as forest fuels load, is a critical factor directly affecting the intensity and size of forest fires [3,4]. Precise fuel load maps facilitate the formulation of targeted forest fire prevention strategies, such as regular clearing of highly FFL areas within forests to reduce the likelihood of ignition from wild sources, thereby mitigating the potential impacts of forest fires [5,6]. They also contribute to the development of targeted forest fire management strategies [7,8].

Forest combustibles mainly consist of biomass and can be categorized into fine fuel and coarse fuels based on the size of the combustible particles. Fine fuel encompasses small branches, leaves, and grass, as well as surface and subterranean organic matter. Coarse fuels include large logs, shrubs, and fallen trees [9]. In our study, fine fuel load (FFL) represents the sum of shrub, herbaceous, FWD (Fine Woody Debris), and litter components within the fuel stratum [10]. Fine fuel possesses a relatively large surface area-to-volume ratio, making it prone to ignition. Once ignited, the compactness and continuity of fine fuel facilitate the sustained spread of fire [11]. When a surface fire ignites the canopy fuels, under the influence of wind, the fire can rapidly expand and ignite additional combustibles, leading to an escalation in the scale of the wildfire. Therefore, an accurate FFL map not only assists in identifying areas of excessive fine combustible accumulation in forests but also guides and plans forest operations to ensure they are kept within reasonable limits. This approach can reduce the likelihood of high-intensity and human-caused forest fires, while acknowledging that moderate natural fires play a significant role in ecosystem management.

The determination of forest combustible materials involves several methodologies, including direct measurement [12], the utilization of allometric equations, and the application of biomass expansion factors [13,14]. The conversion of measurement data to a per-unit-area basis yields the forest FFL unit ( $t \cdot hm^{-2}$ ). The conventional ground-based assessment of forest fine fuel load primarily entails destructive sampling conducted within the forest environment [15] coupled with the establishment of statistical models. Although data garnered from such field surveys are valuable and dependable, their frequent repetition poses challenges due to the time-consuming and labor-intensive nature of the process [16,17].

Estimating FFL through remote sensing offers cost advantages over traditional field surveys, especially when considering large-scale spatial and long-term assessments [18]. The combination of Synthetic Aperture Radar (SAR) images acquired via airborne SAR sensors and semi-empirical algorithms has yielded estimation accuracy values exceeding 70% for both canopy fuel weight and forest biomass. Forest structure indicators obtained from airborne Light Detection and Ranging (LIDAR) data have achieved an R-squared value of 0.84 in estimating forest canopy fuel parameters [19,20]. Yang Chen and collaborators developed a forest surface fuels load prediction model using LIDAR data with an  $R^2$  of 0.61 [21]. The utilization of various airborne radar remote sensing methods for estimating forest flammability has proven to be highly reliable. However, both LIDAR and airborne SAR sensor approaches are costly and difficult to replicate. There is a current need for a cost-effective, repeatable, and large-scale remote sensing method for predicting forest fuels, with cost-effective satellite remote sensing emerging as an ideal choice. Satellite remote sensing can provide extensive and long-term image data, offering the potential for large-scale and long-term FFL estimation [22]. Although many studies have focused on the canopy fuels of forests, ground-level fuels present a unique challenge due to their relative inaccessibility to direct detection via remote sensing technologies. Numerous scholars have attempted to integrate satellite remote sensing technology for estimating forest fine fuel [23–26] and have used this technology to create forest combustible load maps, which have become integral components of comprehensive fire management policies in some regions [27]. Accurately estimating ground-level combustible materials using remote sensing satellites remains a formidable challenge. To address this, our study introduces a machine-learning-based approach for the estimation of FFL. This method employs random convolution to extract and filter FFL-related feature values from satellite imagery. By integrating these extracted

features with ground-surveyed FFL data, we leverage machine learning techniques to construct a comprehensive FFL estimation model. This innovative approach combines the strengths of remote sensing and machine learning.

In recent years, machine learning has emerged as a burgeoning technology. It demonstrates the potential to transform substantial volumes of unstructured image data into actionable quantitative insights. The amalgamation of machine learning methodologies with satellite remote sensing data has been explored to estimate FFL, as evidenced by efforts in this direction [28]. High-resolution images, such as QuickBird, have been demonstrated to be valuable in predicting the load of fine combustibles [25]. Utilizing high-resolution aerial imagery (0.26 m) and employing the Random Forest machine learning approach, precision levels exceeding 80% have been achieved in the estimation of fine fuel in rangeland [29]. These studies highlight the effectiveness of high-resolution imagery and machine learning techniques in accurately estimating FFL in different environments and applications. However, within the scope of this study's knowledge, a research gap persists, particularly in the context of FFL estimation under unfamiliar forest conditions. Furthermore, the dearth of comprehensive large-scale investigations into FFL estimation remains conspicuous.

To address the challenge of rapidly estimating FFL at a large scale, this study aimed to: (1) utilize an unsupervised random convolution approach for FFL estimation from imagery; (2) develop a machine learning model for predicting FFL over a large-scale forest area; (3) predict the distribution of FFL in the study area and generate an FFL map; and (4) provide the study area with reference points for fine fuel management strategies and wildfire prevention strategies based on the FFL map. In summary, this study aimed to combine unsupervised image analysis, machine learning, and geospatial data to efficiently estimate and map FFL, which can be valuable for forest management and wild-fire prevention strategies in the study area.

## 2. Materials and Methods

### 2.1. Study Area

The study area is situated within Changsha City, located in Hunan Province in central-southern China. The geographic coordinates encompass longitude 111°53' to 114°15'E and latitude 27°51' to 28°41'N (Figure 1). Spanning a total land area of 11,819 square kilometers, Changsha City maintains an average elevation of 44.9 m, with elevations ranging from 23.5 m to 1607.9 m. The topography of the region presents distinct characteristics, with mountainous terrain enveloping the eastern and western boundaries, while the central area exhibits flatter landscapes. The prevailing climate of this region is categorized as subtropical monsoon, characterized by prolonged summer and winter seasons and shorter spring and autumn intervals. The bulk of annual precipitation occurs during the summer, contributing to an average annual rainfall of 1361.6 mm within the city's jurisdiction. Rainfall measurements fluctuate between 1358.6 mm and 1552.5 mm across various counties. Notably, the primary vegetation type found in the study area is subtropical evergreen broad-leaved forest. This encompassing flora comprises an impressive diversity of 462 species of evergreen trees, 515 species of deciduous trees, and 414 species of shrubs [30]. The region showcases a rich assortment of vegetation types, reflecting its ecological variety.

In the study area, the forest coverage is 55%, with forests primarily located on the eastern and western sides, as depicted in Figure 2a. These forested regions extend over all mid-to-high-altitude areas, shown in Figure 2b, and include areas where the terrain has gentler slopes, as seen in Figure 2d. The predominant topography in these regions is characterized by hills and mountains. The mountainous environment represents one of the most unique and diverse ecosystems on the planet, exhibiting a wide range of climatic conditions due to its elevation variations, which, in turn, contribute to its rich biodiversity. These ecosystems also serve as crucial water conservation areas, helping to reduce soil erosion, and provide significant cultural and economic values. The urban areas within the study region are in close proximity to these forested areas, where human activities are intensive. Many of the cultural and economic values in these places are highly dependent

on the mountainous ecosystem. While fire is a natural part of forest ecosystems, it is the high-intensity forest fires that pose a particularly destructive impact on these mountainous ecosystems, as opposed to more frequent, lower-intensity fires that can play a beneficial role in some contexts. Accurately understanding the distribution of FFL and implementing appropriate strategies for its clearance to reduce the intensity or prevent forest fires is immensely valuable for maintaining the stability of the mountainous ecosystems in the study area. Therefore, the forest area of Changsha has been selected as the focal area for the prediction and analysis of FFL in this research. Between 2000 and 2018, there were 732 recorded forest fire incidents in the study area, with human activities accounting for over 99% of these occurrences [31]. The prevalence of forest fires in this region may be attributed to frequent agricultural activities and outdoor rituals, further facilitated by a relatively high forest cover of 55%.

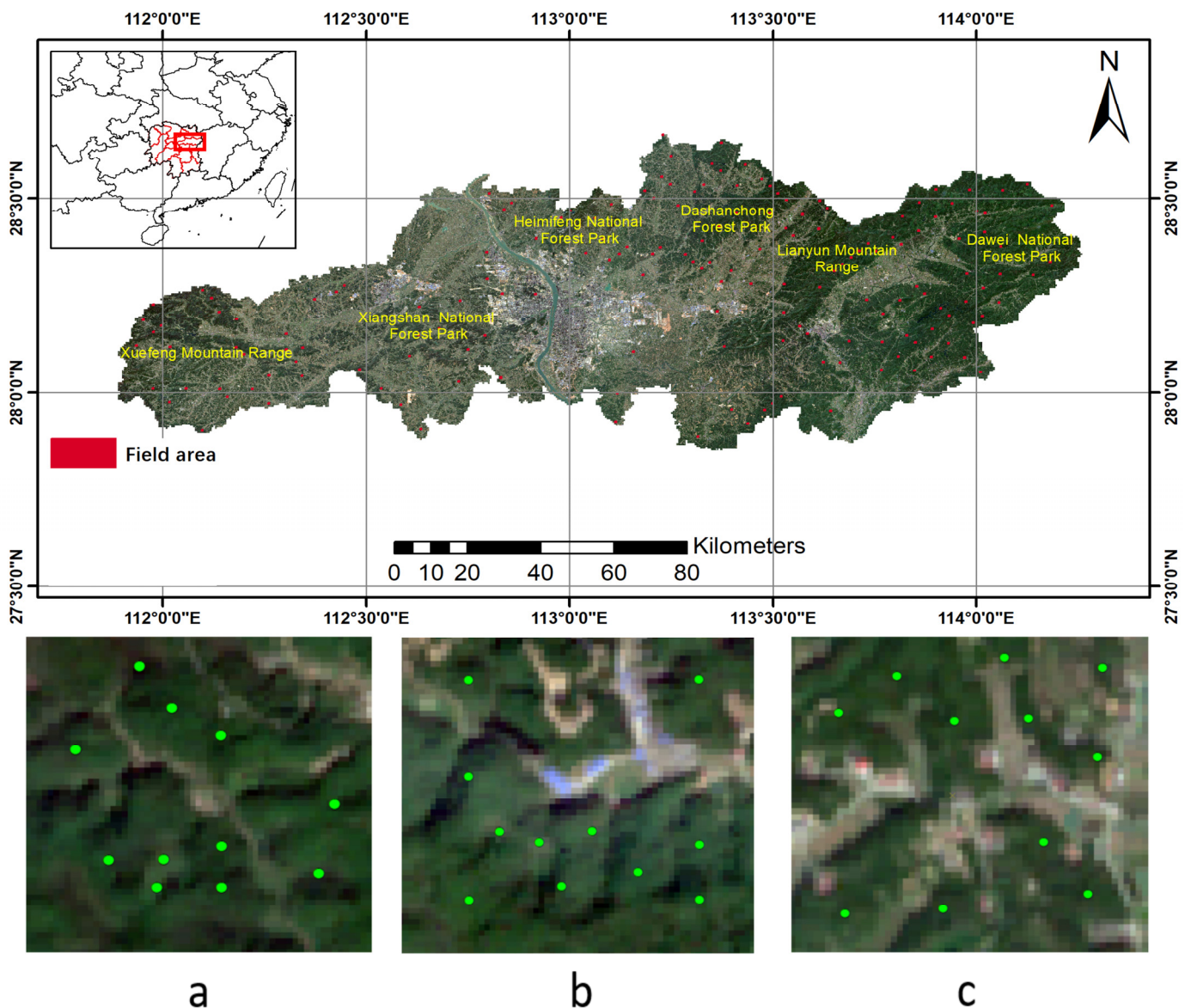


**Figure 1.** Study area. A median-composite B432 true color image of the study area from March to October 2022. Images (a–c) delineate three distinct forest cover scenarios, varying from high to low coverage, with each green dot within these images indicating a specific 2 × 2 m sampling point.

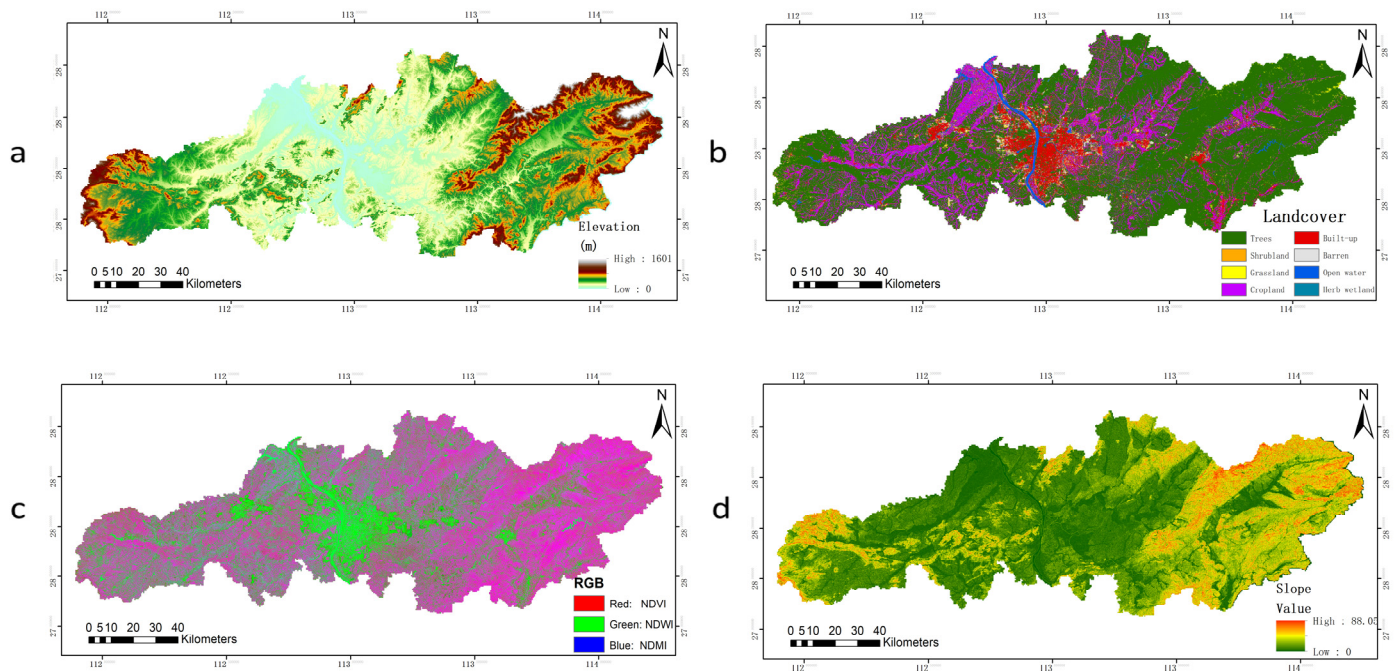


**Figure 2.** (a) Displays a digital elevation map of the study area, (b) shows the land cover map, (c) presents a composite of various vegetation indices where different indices are represented by distinct colors in the RGB spectrum, and (d) illustrates the slope distribution map of the study area.

## 2.2. Field Data

Field data were collected between March and October 2022. This study selected 120 plots within the forested areas of the study area. This study involved a structured approach to data collection within each 500 m rectangular plot. For a comprehensive investigation of fuel material, we randomly selected 11 sampling points across each plot. It is crucial to note that despite the randomness in selection, these points were evenly and representatively distributed within the forested areas of the plots. This strategic approach ensured a balanced representation of the different sections within each plot, enhancing the reliability of our findings. In Figure 1, plots a, b, and c are depicted, where green dots represent the sampling points for fuel material. All plots and sampling points were positioned and corrected using Real-Time Kinematic (RTK) in the GCS2000 coordinate system. Figure 3 presents a field photo and schematic of a sampling point within the plot. Two methods were employed for fine fuel investigation within a  $2 \times 2$  m rectangle at the sampling point: (1) Surface sampling: This sampling targeted the shrub layer. All shrub combustibles on the surface, with each individual shrub under 30 cm in height classified as herbaceous, were measured using a standard tape measure. The collected material was weighed on site using an electronic balance with a precision of 0.01-g. (2) Complete sampling: Based on the surface sampling, this method involved the complete collection of the herbaceous, litter, and FWD. In this context, FWD is a combination of 1 h and 10 h fuels, categorized based on their diameter. The 1 h fuels, consisting of twigs and small branches with a diameter less than 0.25 inches, and the 10 h fuels, composed of slightly larger woody materials up to 1 inch in diameter, were collectively assessed. All materials were weighed on site using an electronic balance with 0.01 g precision. The humus layer fuel was collected after removing any stones and dead branches. Following the method of Tongxin Hu et al. [32], the collected samples were dried to absolute dryness to eliminate the influence of moisture content variability. After measuring the weight of the dried samples, data from all sampling points within each plot were aggregated, and the FFL for each plot was calculated on a per-unit-area basis. The unit of measurement for FFL is tons per hectare ( $t \cdot hm^{-2}$ ).

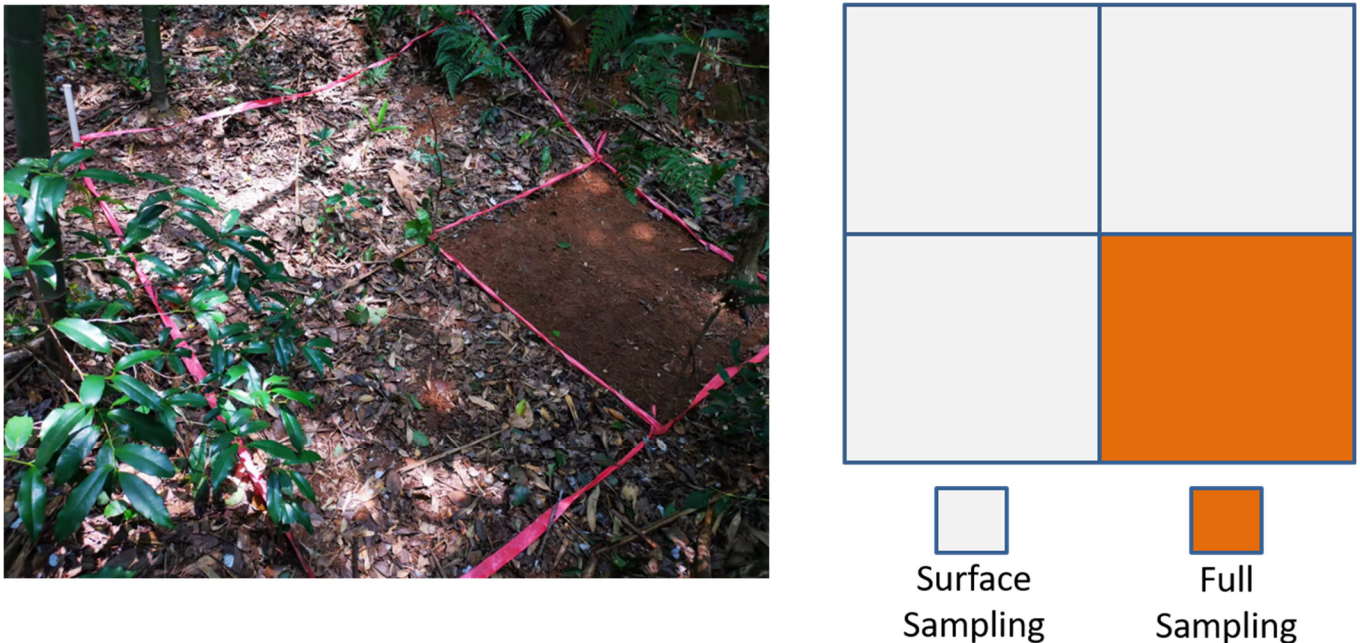


**Figure 3.** Schematic representation of fine fuel sampling points, utilizing two methods to survey fine fuel within the sample plots.

### 2.3. Satellite Imagery Data

The Sentinel-2 satellite, a project of the European Space Agency (ESA), provides imagery spanning thirteen spectral bands encompassing visible light, near-infrared, and short-wave infrared wavelengths [33]. This research utilized Level 2A products from the Sentinel-2A satellite, which have undergone preprocessing steps such as atmospheric correction. The central wavelengths employed in this study include near-infrared (834 nm), blue (496.6 nm), green (560 nm), and red (664.5 nm) bands. Additionally, our study explores the use of common vegetation indices to estimate FFL. These vegetation indices, derived from remote sensing data, likely have an indirect but potentially close correlation with FFL. The perspective of Sentinel-2A suggests a relationship between tree canopy conditions and the surface fuel found in the understory, which is an important aspect to consider in this context. By analyzing the spectral characteristics of the forested areas, these indices may provide insights into the presence and quantity of combustible materials on the forest floor. This research referred to the work of D’Este [27] and employed vegetation indices, namely NDVI (Normalized Difference Vegetation Index), NDWI (Normalized Difference Water Index), and NDMI (Normalized Difference Moisture Index), based on the images with a spatial resolution of 10 m. Clouds and shadows were masked using the QA60 band in the Google Earth Engine (GEE) platform [34]. Median composite images for the period from March to October 2022 were selected. Similarly, this study has leveraged the Advanced Spaceborne Thermal Emission and Reflection Radiometer (ASTER) Global Digital Elevation Model (GDEM), accessible via the GEE platform. ASTER GDEM, a high-resolution global digital elevation model, represents a collaborative development between the Japan Aerospace Exploration Agency (JAXA) and the National Aeronautics and Space Administration (NASA) of the United States. ESA also supplied land cover classification maps for the study area in 2022 with a spatial resolution of 10 m. Figure 2 displays the Sentinel-2A images used in this research, including digital elevation maps, land cover classification maps, false-color images, and images presenting combinations of three vegetation indices.

All data usage and the entire process flow are depicted in Figure 4. This illustration provides a comprehensive overview of the methodologies, data handling, and procedural steps involved in the study.

$$NDVI = \frac{b8 - b4}{b8 + b4} \quad (1)$$

$$NDWI = \frac{b3 - b8}{b3 + b8} \quad (2)$$

$$NDMI = \frac{b8 - b11}{b8 + b11} \quad (3)$$

In the formulas,  $b3$ ,  $b4$ ,  $b8$ , and  $b11$  ( $b11$ , though originally at a spatial resolution of 20 m, has been resampled to a 10 m resolution) correspond to the bands with approximate central wavelengths of 560, 665, 842, and 1610 nanometers, representing the green, red, near-infrared, and shortwave infrared bands, respectively. In this study, the mean values of vegetation indices for all pixels within the sample plots were extracted using the Geospatial Data Abstraction Library (GDAL), a widely used open-source library for reading and writing raster and vector geospatial data formats, in Python.

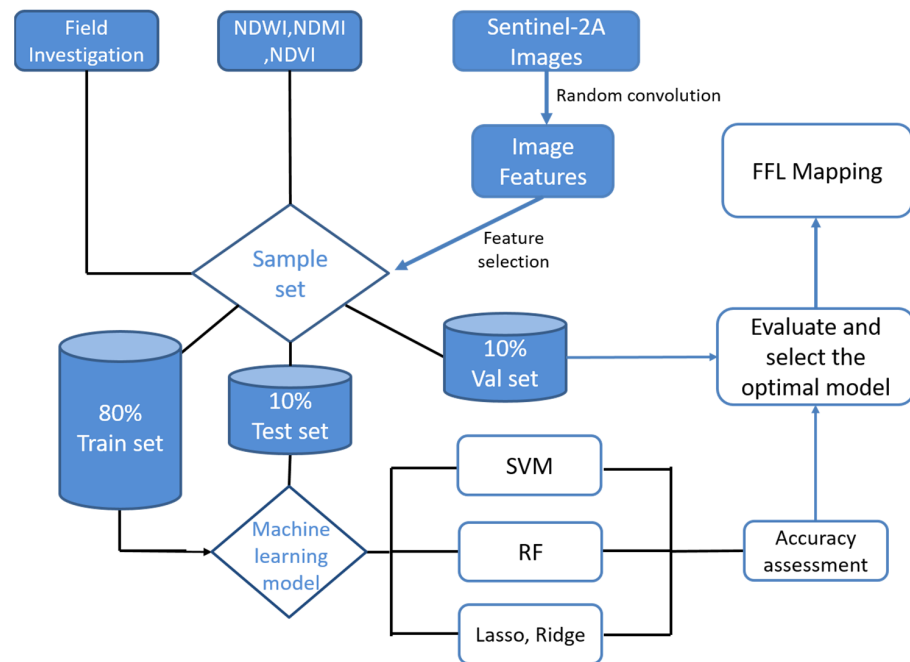


**Figure 4.** Flowchart of the methodology employed in this study.

#### Satellite Image Processing

In this study, the spectral plots' size was defined as 500 m by 500 m. Given the image resolution of 10 m from the Sentinel-2 satellite, the corresponding image size for each plot equates to 50 by 50 pixels. To ensure an accurate alignment between the satellite imagery and the actual surveyed plots, the research utilized ArcGIS software (version 10.8). Tools within the Data Management Tools and Analysis Tools, specifically the Clip, Buffer, and Minimum Bounding Geometry tools, were employed to calculate the minimum bounding rectangle around the center point of each field plot. This procedure facilitated the precise cropping of Sentinel-2A imagery to obtain images corresponding to each respective plot. To prevent the machine learning models from capturing irrelevant features during training, which could lead to model divergence or overfitting, land cover maps were used to create labels for non-forest land types such as buildings, bare land, roads, water bodies, and others. These labels were used to mask out the non-forest areas in the images. Figure 5 illustrates the process of creating non-forest land label masks using land cover maps. Prominent

features such as bodies of water, buildings, and bare ground in the imagery were masked. In total, 120 Sentinel-2A images corresponding to surveyed plots were used in this study. These images were randomly split into training, testing, and validation sets in an 8:1:1 ratio.

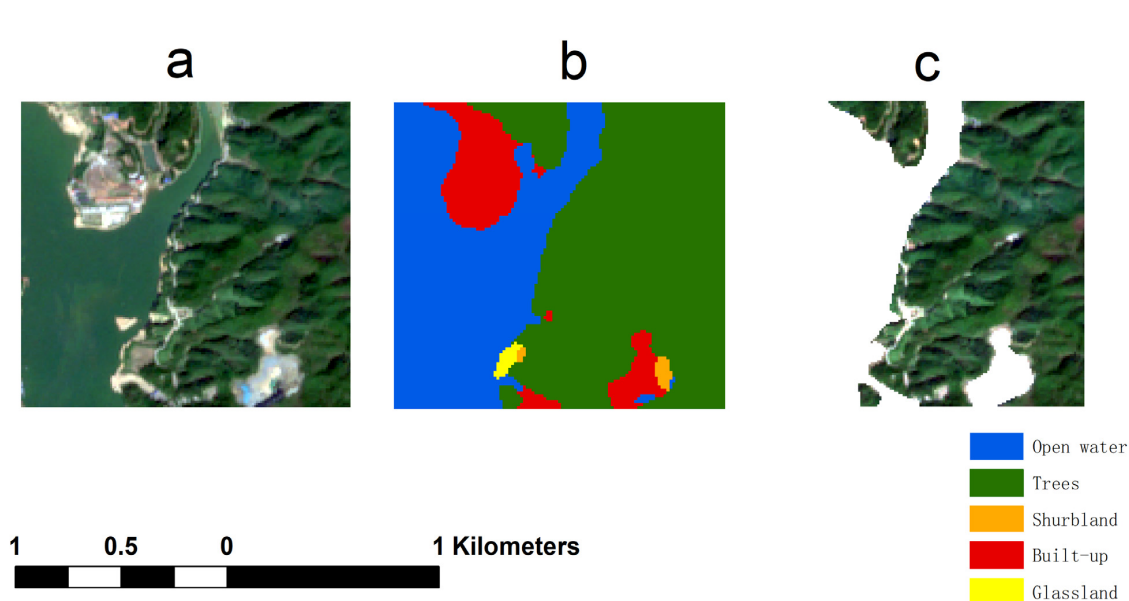


**Figure 5.** The process of image mask processing can be outlined as follows: (a) shows the original image, (b) displays the land cover map, and (c) depicts the image after masking.

#### 2.4. Random Convolution

The process of estimating FFL necessitates the execution of linear regression on continuous data values. Hence, in this study, a random convolution algorithm was effectively harnessed to extract essential features from images. These extracted features, in turn, were instrumental in the construction of an FFL estimation model. The employed random convolution algorithm in this study operates under an unsupervised framework. This algorithm facilitates the random selection of convolutional kernels from a dataset of images for the explicit purpose of feature extraction. The inherent advantage of this algorithm lies in its capacity to capture the intrinsic features of images more effectively compared to predefined kernels. The acquired features are then transformed into interpretable and quantifiable feature vectors, which subsequently serve as building blocks for shaping the FFL estimation model. To operationalize random convolution, this study leveraged the capabilities of PyTorch, an open-source machine learning library known for its flexibility and efficiency in modeling and training algorithms, and capitalized on GPU (Graphics Processing Unit) acceleration, a technology that significantly speeds up computational processes, for enhanced computational efficiency.

We carried out feature extraction using the random convolution algorithm from a given set of images, as depicted in the schematic diagram in Figure 6. Random convolution is an algorithm designed to generate variable features for each image in a dataset, providing a flexible approach to feature extraction [35]. This process starts with a collection of  $N$  images, from which the algorithm randomly selects  $K$  patches. Subsequently, each patch undergoes a process of matrixization and whitening, leading to the derivation of corresponding convolutional kernels. These kernels are then applied to perform convolution calculations on each image, generating  $K$  non-linear activation maps for each image. Once these activation maps are obtained, the algorithm computes their mean-over-pixel values to create a  $K$ -dimensional feature vector for each image. For each plot, the corresponding  $K$ -dimensional feature vector derived from the satellite imagery, along with the FFL measurements, will be inputted into the machine learning model as independent and dependent variables, respectively.

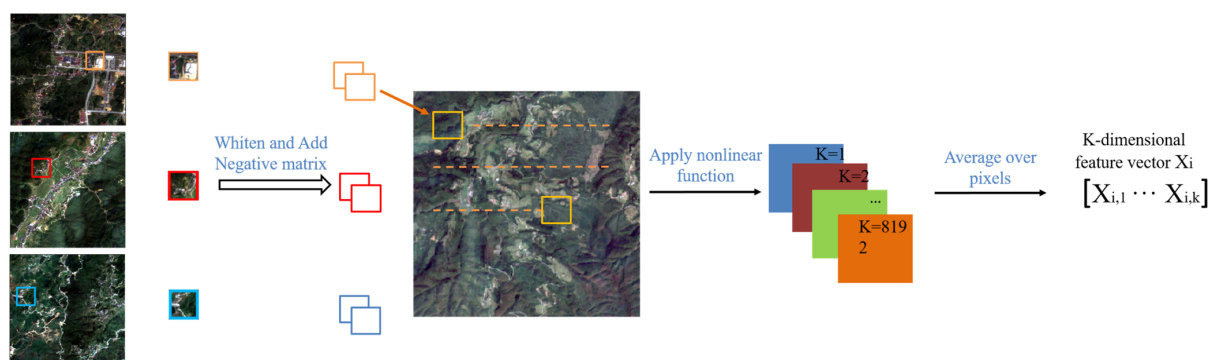


**Figure 6.** The provided schematic diagram illustrates the process of feature extraction performed by the random convolution algorithm from a given set of images.

In summary, convolution identifies and extracts specific textures, colors, and patterns from images, quantifying and normalizing these features. There may exist a certain correlation between the processed features and the FFL. The approach of machine learning involves leveraging this correlation between features and FFL to establish a model that uses these features to predict FFL.

The kernel size in the convolution process is a crucial variable that directly affects feature extraction. Choosing an appropriate kernel size can effectively enhance the accuracy of FFL estimation. Therefore, we conducted tests on four different kernel sizes with four different models, and utilized  $R^2$  as the primary metric to evaluate how kernel size affects model performance.

### 2.5. Machine Learning Model

We employed four regression models to estimate FFL in this study: Random Forest (RF), Support Vector Machine (SVM), Ridge Regression (Ridge), and Lasso Regression (Lasso). Machine learning has found extensive application in wildfire science and management [36]. Among these models, RF and SVM are common choices for wildfire management. RF is an ensemble learning method known for its exceptional performance in handling large-scale data and high-dimensional features. SVM, when adapted as SVR (Support Vector Regression), is effective for high-dimensional data. This approach is particularly suited to our context where the dependent variable is continuous, allowing us to leverage the algorithm's capabilities for regression rather than classification. Ridge Regression incorporates L2 regularization to address multicollinearity, offering better solutions to overfitting issues. Lasso Regression, on the other hand, employs L1 regularization for feature selection and parameter shrinkage.

#### 2.5.1. Model Parameter Setting

In our research's early stages, we tested the influence of parameter selection on four models. On our dataset, the default parameters seemed to be the best choice, but adjusting some parameters might still enhance the models' potential performance. The RF model was implemented using the RandomForestRegressor from the scikit-learn library. To tune the RF model, 'n\_estimators' and 'random\_state' parameters were set. 'n\_estimators', the number of decision trees, controls model complexity; 'random\_state' is a seed for controlling sampling randomness, ensuring experimental reproducibility. 'n\_estimators' was used with the default value of 500, and 'random\_state' was set to 200. The SVM model was implemented using LinearSVR from the scikit-learn library, setting its kernel function to linear, with other parameters at default. Ridge and Lasso models were implemented using scikit-learn's Lasso and Ridge, respectively. The 'alpha' parameter, representing the strength of the regularization term, affects the model's fitting capability. 'Alpha' was set to the default value of 0.1.

It is important to emphasize that all code snippets mentioned adhere to the Python programming language and rely on the scikit-learn library to facilitate machine learning operations.

### 2.5.2. Model Performance Metrics

In order to conduct a comprehensive evaluation of the RF, SVM, Ridge, and Lasso models, this study adopted a set of performance metrics aimed at assessing the accuracy of these models. The chosen metrics encompass the following: 1. Root Mean Absolute Error (RMAE) (4); 2. Root Mean Square Error (RMSE) (5); 3. Coefficient of Determination ( $R^2$ ) (6); and 4. Correlation Coefficient ( $R$ ) (7).

$$RMAE = (1/n) \times \sum |y_i - p_i| \quad (4)$$

$$RMSE = \sqrt{\frac{\sum_{i=1}^n (y_i - p_i)^2}{n}} \quad (5)$$

$$R^2 = 1 - \frac{\sum_{i=1}^n (y_i - p_i)^2}{\sum_{i=1}^n (y_i - \bar{p}_i)^2} \quad (6)$$

$$R = \frac{\sum_{i=1}^n (p_i - \bar{p}_i)(y_i - \bar{y}_i)}{\sqrt{\sum_{i=1}^n (p_i - \bar{p}_i)^2 \sum_{i=1}^n (y_i - \bar{y}_i)^2}} \quad (7)$$

In the provided formulas,  $y_i$  represents the true value,  $\bar{y}_i$  represents the mean of the true values,  $p_i$  represents the predicted value, and  $\bar{p}_i$  represents the mean of the predicted values.

## 3. Results

### 3.1. Field Data Analysis

The boxplot analysis reveals that the distribution of FFL across the study plots ranges from 0.55 to 106.75 tons per hectare ( $t \cdot hm^{-2}$ ), with an average of 13.5  $t \cdot hm^{-2}$ . The individual points depicted as circles in Figure 7b represent the outliers, which are predominantly situated above 38.7  $t \cdot hm^{-2}$ , indicating specific plots where the FFL is unusually high. The distribution of the plot data exhibits a right-skewed tendency, where the sample mean is lower than the median, and the median is lower than the mode. This indicates a prevalence of plots with lower fuel loads. These observations are detailed in Figure 7a. Consequently, it can be inferred that the majority of FFL are concentrated within the range of 3.52 to 16.01  $t \cdot hm^{-2}$ , as demonstrated in Figure 7b.

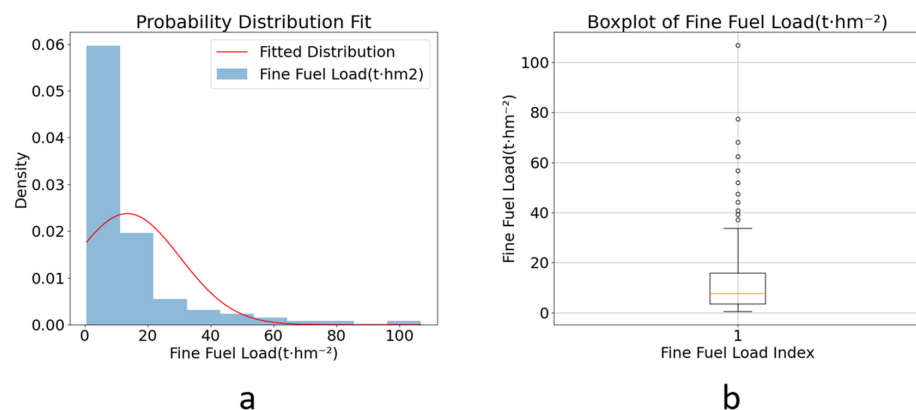


**Figure 7.** Distribution plot of FFL within the sample plots. (a) Probability distribution plot of FFL within the sample plots, with a red line depicting the probability distribution curve; and (b) is the box plot of the sample data.

### 3.2. Vegetation Index Model

In this study, matrices for the NDVI, NDWI, and NDMI were computed. The mean values of these matrices were then inputted into the training process for the machine learning models. The accuracy of four different linear regression models in estimating FFL using these three distinct vegetation indices is presented in Tables 1–3.

**Table 1.** FFL prediction accuracy under NDVI.

Model	RMSE	RMAE	R	R <sup>2</sup>
RF	14.13	9.4	0.532	0.272
SVM	12.13	6.97	0.41	0.01
Ridge	8.5	6.59	0.51	0.144
Lasso	9.73	7.93	0.453	0.026

**Table 2.** FFL prediction accuracy under NDWI.

Model	RMSE	RMAE	R	R <sup>2</sup>
RF	15.69	9.16	0.67	0.427
SVM	12.14	6.97	0.406	0.01
Ridge	11.01	7.55	0.601	0.129
Lasso	9.79	8.01	0.464	0.013

**Table 3.** FFL prediction accuracy under NDMI.

Model	RMSE	RMAE	R	R <sup>2</sup>
RF	8.31	7.14	0.624	0.386
SVM	12.16	6.92	0.454	0.01
Ridge	8.66	11.03	0.605	0.128
Lasso	9.61	7.17	0.07	0.003

From the predicted results, it is evident that only RF exhibited reasonable predictive performance when using vegetation indices for FFL estimation. Among them, NDWI performed the best, with an R<sup>2</sup> of 0.427 and an R of 0.67. NDMI followed closely, with an R<sup>2</sup> of 0.386 and an R of 0.624. NDVI, on the other hand, performed the worst among the three vegetation indices. The superior performance of the NDWI in this study can be attributed to the correlation between the water content of the forest canopy's leaves and the accumulation of ground-level combustible materials. A higher water content in the upper vegetation's leaves may influence light penetration and microclimatic conditions, thereby indirectly affecting the growth of ground-level vegetation and the accumulation of combustible materials. Conversely, the NDVI exhibited the least effectiveness among the three vegetation indices. This suggests that NDVI may not have a significant correlation with the accumulation of lower-layer combustibles. NDVI primarily indicates vegetation health and density, which might not directly relate to the quantity or condition of fine fuel materials accumulated on the forest floor. Therefore, it seems that NDVI appears to be less suited for FFL estimation. Consequently, we opted for RF using the NDWI index to generate the FFL map.

### 3.3. Machine Learning Models

#### 3.3.1. Feature Vector Selection

In this study, we aimed to investigate the impact of convolution kernel size on FFL estimation. Consequently, we employed four different kernel sizes, namely 2 pixels, 4 pixels, 8 pixels, and 16 pixels, to extract feature vectors.

The analysis shows that most feature vectors have correlations with FFL below 0.3, regardless of the kernel size. True-color images have the fewest high-correlation feature vectors, while false-color images show the highest number of feature vectors with correlations above 0.5 at 4- and 8-pixel kernel sizes. For the B8432 composite image, the most significant correlations are found at kernel sizes of 4, 8, and 16 pixels. Considering both the magnitude and quantity of correlations, false-color and B8432 composite images may yield higher accuracy in FFL estimation. To improve precision and speed in model predictions, feature vectors with correlations below 0.3 will be excluded from training, focusing only on those exceeding 0.3. The correlation details between feature vectors and FFL for different kernel sizes are provided in Tables 4–6.

**Table 4.** The correlation between the feature vectors extracted using different convolution kernel sizes under the B8432 image.

Range of Correlation Values	Convolution Kernel Size (Pixel)			
	2	4	8	16
0.5–0.6	6	36	32	59
0.4–0.5	19	951	700	558
0.3–0.4	1267	856	981	794
0.2–0.3	1265	806	864	866
0~0.2	5603	5544	5616	5916

**Table 5.** The correlation between the feature vectors extracted using different convolution kernel sizes under the true-color images.

Range of Correlation Values	Convolution Kernel Size (Pixel)			
	2	4	8	16
0.5–0.6	0	0	1	11
0.4–0.5	1	660	771	588
0.3–0.4	186	1137	1112	998
0.2–0.3	2207	874	786	796
0~0.2	5786	5522	5523	5800

**Table 6.** The correlation between the feature vectors extracted using different convolution kernel sizes under the false-color images.

Range of Correlation Values	Convolution Kernel Size (Pixel)			
	2	4	8	16
0.5–0.6	4	77	48	9
0.4–0.5	204	1027	718	535
0.3–0.4	1416	896	988	998
0.2–0.3	1095	717	851	874
0~0.2	5448	5476	5588	5777

### 3.3.2. Impact of Convolutional Kernel Size on Model Accuracy

The influence of convolution kernel size on model accuracy is evident in this study, with Tables 7–9 presenting the detailed results of these effects. With a kernel size of two pixels, the accuracy of the estimation results was generally lower. Under this kernel size, the Lasso model performed the best, achieving its highest estimation accuracy on the B843 imagery with an  $R^2$  of 0.613, as shown in Table 9. When the kernel size was increased to four pixels, the RF model achieved the highest estimation accuracy on the B8432 composite imagery, with an  $R^2$  of 0.656, as seen in Table 7. With a kernel size of 16 pixels, Lasso obtained results on the B432 imagery, as indicated in Table 8, however, it was the RF model with a two-pixel convolution that achieved the highest  $R^2$  value of 0.515. This study suggests that smaller kernel sizes (two pixels and four pixels) may be more advantageous for extracting features relevant to FFL. However, as the kernel size increased to 8 pixels or more, the predictive performance of all four models generally began to decline, with the exception of the Lasso model under the B432 imagery, where its performance improved with increasing kernel size, as shown in Table 8.

**Table 7.** Coefficient of determination ( $R^2$ ) for Predictions of different models using different convolutional kernel sizes on B8432 images.

Models	Convolution Kernel Size (Pixels)			
	2	4	8	16
RF	0.326	0.656	0.626	0.167
SVM	0.284	0.323	0.386	−0.165
Ridge	0.332	0.275	0.03	0.06
Lasso	0.352	0.257	0.47	0.42

**Table 8.** Coefficient of determination ( $R^2$ ) for predictions of different models using different convolutional kernel sizes on true-color images.

Models	Convolution Kernel Size (Pixels)			
	2	4	8	16
RF	0.515	0.458	0.453	0.034
SVM	0.191	0.342	0.283	0.161
Ridge	0.219	0.247	−1.196	−0.692
Lasso	0.24	0.385	0.335	0.45

**Table 9.** Coefficient of determination ( $R^2$ ) for predictions of different models using different convolutional kernel sizes on false-color images.

Models	Convolution Kernel Size (Pixels)			
	2	4	8	16
RF	0.402	0.513	0.386	0.155
SVM	0.361	0.555	0.106	−0.36
Ridge	0.322	0.252	0.329	−1.05
Lasso	0.613	0.364	0.329	0.182

The information encapsulated in Tables 7–9 casts a light on the outcomes yielded by various models when subjected to diverse convolutional kernel sizes. The assessment of these outcomes, grounded in the  $R^2$  metric, underscores the following insights: Amongst the true-color images, the RF model emerges as the optimal performer in predicting FFL with a kernel size of four pixels.

In our study, the Lasso model showed superior performance in predicting FFL for false-color images with a two-pixel kernel size. Generally, an increase in kernel size led to decreased predictive performance across most models, except for Lasso in true-color images, where larger kernels improved performance. The RF model excelled with B8432 imagery using four- and eight-pixel kernels, as evidenced by lower RMSE and RMAE values, indicating higher accuracy. Overall, most models achieved their best predictive results with kernel sizes of two or four pixels.

### 3.3.3. Estimation of FFL and Model Selection

For the B8432 imagery, the Random Forest (RF) model exhibited its best performance with a convolution kernel size of four pixels. Similarly, for the B843 imagery, the RF model achieved optimal performance with a kernel size of four pixels. In the case of the B432 imagery, the Lasso model performed best with a kernel size of 16 pixels.

This study found that RF and Lasso are the most suitable models for FFL estimation, with RF excelling in both true-color and false-color images, achieving  $R^2$  values of 0.453 and 0.602, respectively. Lasso performs better on the false-color image, showing an improvement of 0.228 in  $R^2$  compared to the true-color image. Ridge and SVM, however, displayed lower  $R^2$  values, indicating they may be less suitable for this task. Considering combined model performance measures such as RMSE, RMAE, R, and  $R^2$ , RF is optimal for true-color images and B8432 images, while Lasso is best for false-color images. The best FFL estimation results and corresponding kernel sizes for the four models on B8432, true-color, and false-color images are detailed in Table 10 and Figure 8, Table 11 and Figure 9, and Table 12 and Figure 10, respectively.

**Table 10.** Best predictive accuracy results of different models on B8432 images.

Models	RMSE (t/hm <sup>2</sup> )	RMAE (t/hm <sup>2</sup> )	R	R <sup>2</sup>
RF	5.847	4.938	0.836	0.656
SVM	10.785	9.06	0.69	0.386
Ridge	9.74	7.44	0.59	0.332
Lasso	11.17	7.756	0.688	0.47

**Table 11.** Best predictive accuracy results of different models on true-color images.

Models	RMSE (t/hm <sup>2</sup> )	RMAE (t/hm <sup>2</sup> )	R	R <sup>2</sup>
RF	7.79	6.518	0.89	0.39
SVM	12.95	10.80	0.585	0.342
Ridge	14.14	18.75	0.533	0.247
Lasso	9.76	7.36	0.686	0.438

**Table 12.** Best predictive accuracy results of different models on false-color images.

Models	RMSE (t/hm <sup>2</sup> )	RMAE (t/hm <sup>2</sup> )	R	R <sup>2</sup>
RF	6.78	5.13	0.894	0.537
SVM	18.66	14.88	0.781	0.355
Ridge	7.87	6.79	0.779	0.322
Lasso	6.21	4.72	0.823	0.612

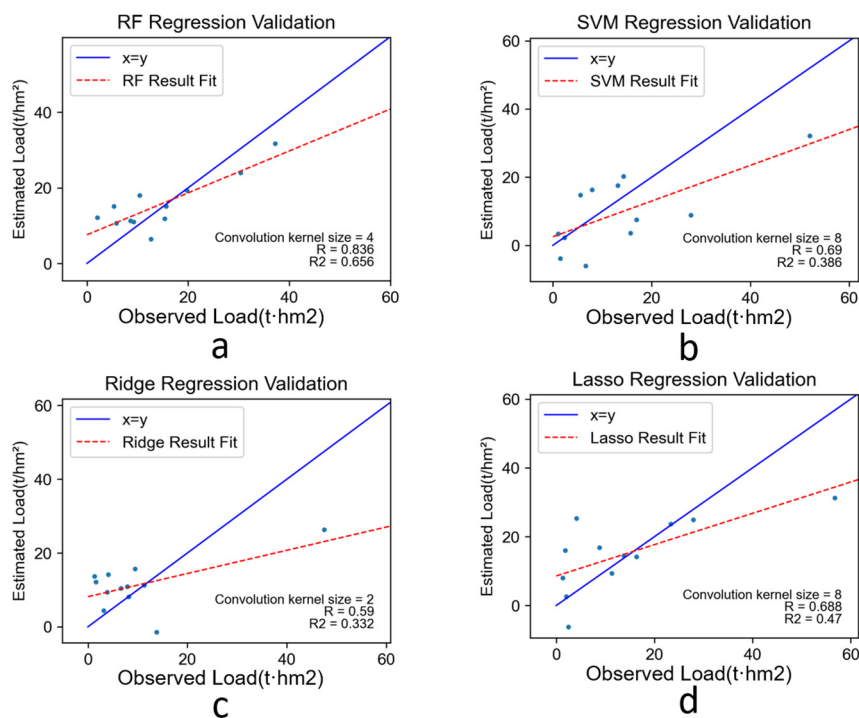


**Figure 8.** Comparison of validation set accuracy for different models on B8432 composite images. (a) Represents the best result achieved using the RF model, (b) represents the best result obtained with the SVM model, (c) represents the best result from the Ridge model, and (d) represents the best result using the Lasso model.

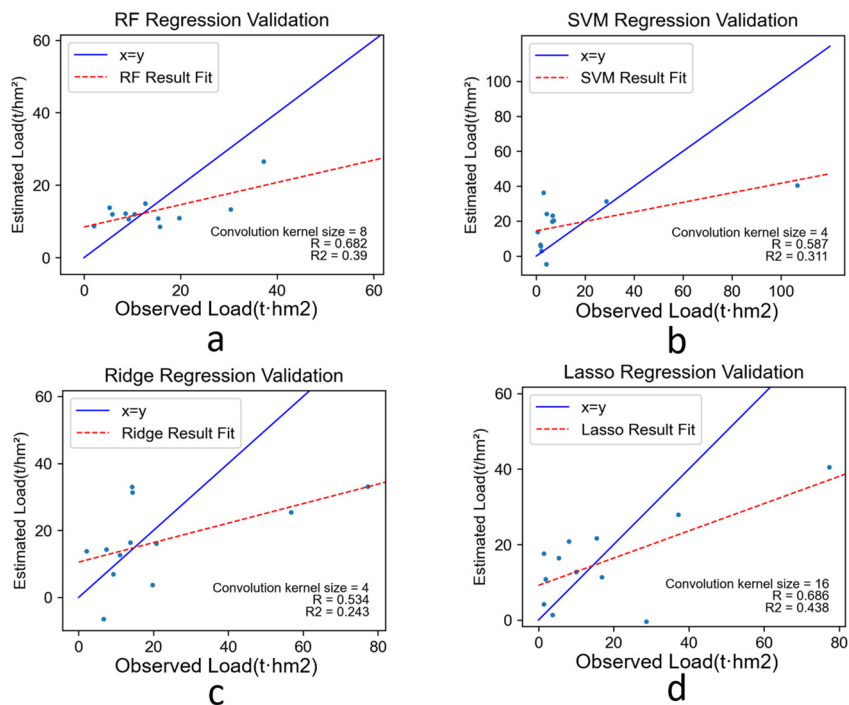


**Figure 9.** Comparison of validation set accuracy for different models on true-color composite images. (a) Represents the best result achieved using the RF model, (b) represents the best result obtained with the SVM model, (c) represents the best result from the Ridge model, and (d) represents the best result using the Lasso model.

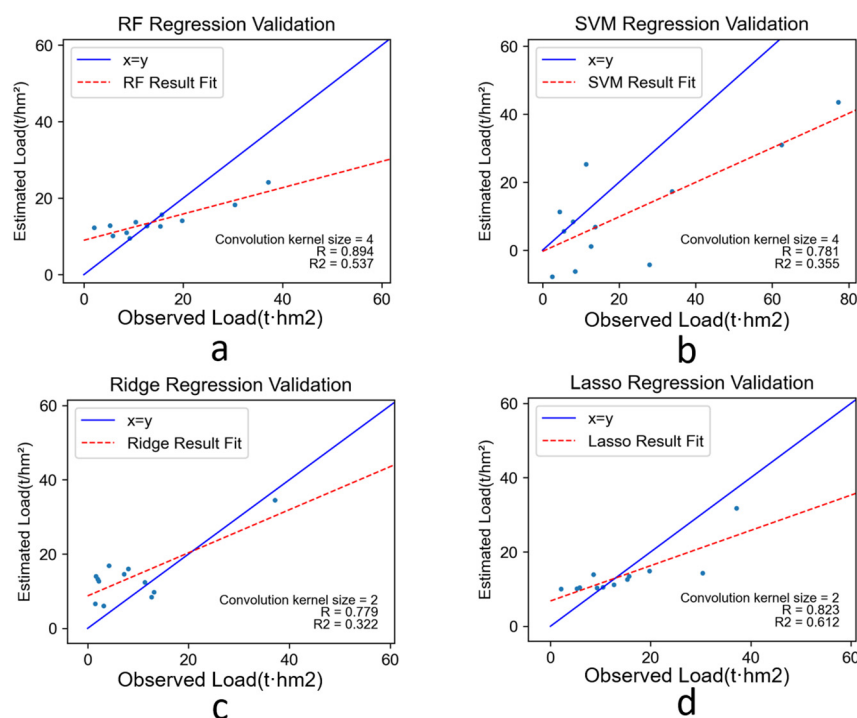


**Figure 10.** Comparison of validation set accuracy for different models on false-color composite images. (a) Represents the best result achieved using the RF model, (b) represents the best result obtained with the SVM model, (c) represents the best result from the Ridge model, and (d) represents the best result using the Lasso model.

### 3.3.4. FFL Map

Based on the performance metrics, this study has chosen RF as the prediction model for FFL using the B8432 image, Lasso as the prediction model for true-color and false-color images, and NDWI for predicting and generating the FFL map for the study area.

The generated FFL maps are showcased in Figure 11, where a red box highlights a detailed segment of the FFL map. In Figure 11, the two red boxes mark distinct terrain features in the study area. The first red box represents a higher-altitude mountainous region with dense forest coverage, where FFL values are elevated. The second red box indicates a lower-altitude area at the interface between forests and human settlements, where FFL values are influenced by human activities. The FFL results using the B8432 combination show differences in FFL distribution across the two regions, as seen in Figure 11d. In the high-altitude area marked by the first red box, the B8432 bands may capture more features associated with higher fuel loads due to lush vegetation. In the second red box, the impact of human activities suggests that FFL estimation should account for discontinuities in fuel distribution caused by farming or construction activities. In terms of overall numerical predictions, the FFL estimate from the B8432 combination is higher than that from the true-color image, which, in turn, is higher than that from the false-color image. Regarding visual interpretation, the FFL map predicted using NDWI appears somewhat chaotic. While it may contain erroneous results in comparison to the other FFL maps, its general predictions align with the others. It is clear that higher FFL values are primarily found in forested areas within the study region. Specifically, these higher FFL values are more prevalent in the eastern part of the study area, which is characterized by mid-to-high altitudes and a denser forest cover. Conversely, lower FFL values are observed mainly in the central and southern regions, where the landscape comprises more buildings and farmlands. This pattern suggests a strong correlation between FFL distribution and both elevation and land cover, with forested and higher altitude areas in the east showing greater FFL.

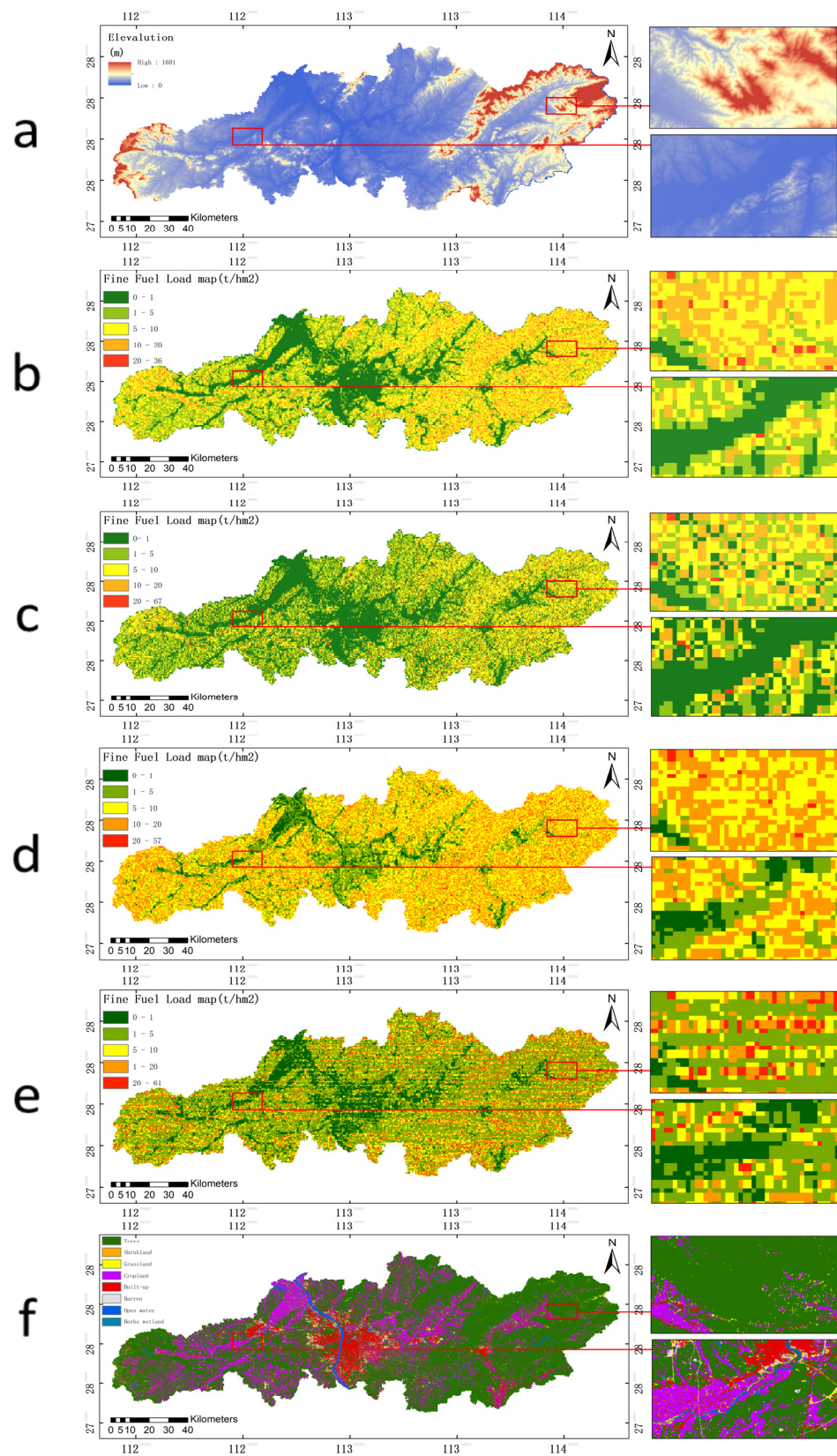


**Figure 11.** FFL maps created using different images. (a) Represents DEM image, (b) represents FFL established using true-color imagery, (c) represents FFL established using false-color imagery, (d) represents FFL established using the B8432 combination, (e) represents FFL established using NDWI imagery, and (f) represents the land cover map.

## 4. Discussion

### 4.1. Estimation Accuracy of Machine Learning Model Based on Random Convolution

In this study, feature vectors were obtained from remote sensing images using random convolution to establish models for estimating FFL. Through performance evaluation, RF demonstrated the best predictive performance on the B8432 image, with an RMSE of 5.847 t/ha and an  $R^2$  of 0.656. The superior performance of RF model in our study can be attributed to several factors. First, its ability to handle high-dimensional data is particularly crucial for the complex features extracted from satellite imagery. Second, the ensemble learning characteristic of RF is adept at capturing complex and non-linear relationships within the data. Finally, the use of multiple decision trees in RF contributes to its robustness against outliers and noise, making it highly effective for analyzing for predicting FFL based on diverse and intricate datasets. Subsequently, the optimal models corresponding to the four images were used to predict and create FFL maps for the study area with a spatial resolution of 500 m. Although many studies have focused on the canopy fuels of forests, ground-level fuels present a unique challenge due to their relative inaccessibility to direct detection via remote sensing technologies. This attribute renders research on ground-level fuels less prevalent and more complex. In our study, we specifically concentrated on enhancing the quantification capabilities for these challenging-to-predict ground fuels. Our results indicate that the combination of random convolution with remote sensing imagery and machine learning can effectively predict Forest FFL on a larger scale. This approach offers a promising outlook for research in this field, demonstrating the potential of advanced remote sensing and analytical techniques in overcoming the challenges associated with ground-level fuel quantification in forested areas. Despite the indirect nature of remote sensing data, these techniques can still yield accurate FFL predictions by capturing key indicators of fuel presence and conditions, such as vegetation density, moisture content, and other environmental factors that influence fuel accumulation.

The findings of this study align harmoniously with the investigations conducted by Labenski [37]. In their work, they embarked on modeling and mapping surface fuels in mixed forests, employing the amalgamation of airborne LiDAR and Sentinel-2 data. Notably, their simulation outcomes exhibited  $R^2$  values ranging from 0.55 to 0.64 for shrub fuels' load estimation and from 0.27 to 0.41 for fine dead fuels' load estimation. By way of comparison, the current study attained a heightened level of accuracy in FFL estimation, conceivably attributable to the inherent strengths and potential of the feature vectors extracted through the process of random convolution. These feature vectors manifest an innate affinity for capturing intricate linear relationships between specific environmental variables and forest fuel characteristics, thus conferring an advantage. Similarly, Arellano-Perez [38] harnessed Sentinel-2 data and harnessed machine learning techniques for estimating surface fuel loads within pine forests situated in northwestern Spain. Their predictive  $R^2$  values spanned the spectrum from 0.02 to 0.12. This limited range could potentially be attributed to the relatively modest correlations observed between remote sensing variables and fuel loads. In stark contrast, the application of random convolution in this study yielded an ample array of feature vectors drawn from Sentinel-2 images, ultimately unlocking a greater reservoir of latent image features. The resultant effect was a discernible enhancement in performance, a testament to the capacity of the adopted methodology. Specifically, the convolution filtering technique employed in this study significantly improved the FFL estimation by effectively utilizing canopy reflectance data. This approach provides an indirect yet more effective means of assessing surface fuel conditions beneath the canopy. This approach potentially captures subtle variations in how light interacts with the forest canopy and ground, which may contribute to a more accurate estimation of the location and amount of fuel on the forest floor. The advanced processing of these reflectance data through convolution filtering allows for a more detailed and accurate representation of the complex interaction between forest canopy characteristics and the underlying fuel conditions.

#### 4.2. The Importance of FFL Map

Effectively managing and controlling the size and intensity of forest wildfires within the wildland–urban interface presents a significant challenge in the study area. In the realm of fire management, an emphasis on prevention, rather than post-fire rescue operations, is deemed crucial [39]. Once fine fuel is ignited, surface fires can easily spread to the canopy, leading to more active crown fires, which result in wildfires that are much more difficult to control. The transition from surface to crown fires represents a significant escalation in fire behavior, intensity, and potential for destruction. During the prevention phase, the precise mapping of forest FFL assumes pivotal importance, aiding in the formulation of regulations aimed at curtailing fuel accumulation [40] and mitigating the heightened fire risk attributed to fuel buildup [41]. Additionally, these data are crucial during fire suppression activities, particularly when a fire is detected in areas with heavy surface fuels, as they are vital for strategizing firefighting efforts and ensuring firefighter safety. It is worth noting that fine fuel holds the distinction of being the most easily ignitable type of forest fuel [42], playing a crucial role as the carrier for fire propagation [43]. Past research studies have endeavored to delineate forest fuel types or estimate fuel loads through diverse methodologies, encompassing radar, remote sensing, and biophysical models [19,44–47]. However, previous approaches faced limitations in scope, time, and resource demands. This study represents a significant advancement, as it harnesses the overhead 2D perspective of Sentinel-2 to gain enhanced information on forest surface fuels. The breakthrough in FFL estimation was achieved by applying a convolutional filtering method to specific image subsets, demonstrating the effectiveness of integrating remote sensing imagery with machine learning techniques in the context of our study area. This study heralds a significant advancement in fire management strategies by providing credible decision support information through the mapped FFL. This approach enables more targeted and effective fire management activities by offering precise data on forest fuel distribution and potential fire risks.

#### 4.3. The Impact of Convolution Kernel Size on Model Accuracy

In this study, which evaluated RF, SVM, Ridge, and Lasso models, it was observed that the RF and Lasso models exhibited better performance. The test results indicate that the RF model is better suited for building FFL models using the B8432 band combination and true-color imagery. In contrast, the Lasso model is found to be more appropriate for building FFL models exclusively using false-color band combinations. Although differences between different models led to variations in predictive accuracy, the size and number of convolution kernels extracted during the random convolution process may have a more significant impact on the predictive accuracy of the models. This study selected four different sizes of convolution kernels ( $2 \times 2$  pixels,  $4 \times 4$  pixels,  $8 \times 8$  pixels,  $16 \times 16$  pixels), with a fixed number of 8192 kernels for each size. Not all feature vectors extracted by these convolution kernels need to be input into the machine learning models. This study aimed to investigate the convolution kernel-related parameters that are suitable for FFL models by controlling the kernel size and the number of input feature vectors. The results of this research suggest that when the convolution kernel size is set to two pixels or four pixels, the predictive results come close to the optimal level. While the image features of fine combustible materials are extracted more effectively with smaller convolution kernels, it is important to note that these are indirect measures. The images primarily capture overstorey tree canopy conditions, which are correlated with surface fuel conditions in this system, rather than directly measuring the fine combustible materials. In contrast, larger convolution kernels did not yield as favorable results in the feature extraction process.

#### 4.4. FFL Mapping and Wildfire Risk Management Strategies

In the study area, human settlements and zones of human activity, which can potentially initiate wildfires, are closely adjacent to forest boundaries. While these activities heavily rely on the various values of the mountainous ecosystem, they also pose an increased risk of wildfires, particularly in terms of ignition sources. Local rituals like burning offerings and setting off fireworks contribute to this risk. In mid-to-low-altitude areas, exemplified by the second red box in Figure 11, where human activity is common and the overlap between urban and forested areas is considerable, it is crucial to implement strategies such as educating the local populace about fire prevention and rigorously controlling anthropogenic ignition sources. This includes restricting the burning of crop residues and other open flames to reduce the accumulation of FFL, which might be the most cost-effective strategy. Meanwhile, in the high-altitude regions indicated by the first red box in Figure 11, it is imperative to focus on ecological management practices such as sustaining natural firebreaks and removing combustible materials like dead branches and fallen leaves, particularly during periods susceptible to wildfires. These strategies are integral for mitigating fire hazards and managing wildfire risks effectively. These activities are crucial to effectively manage and reduce the risk of wildfires. The key areas for fire prevention, as indicated by the FFL maps, are predominantly located in the mid-to-high elevations of the eastern region, where prioritizing fuel hazard mitigation activities, such as establishing fuel breaks [48], is essential. Regular updates of FFL maps and ground validation are necessary in both the lower and higher altitude areas to ensure the accuracy and effectiveness of the management strategies. By prioritizing fire prevention in areas with high human activity and adjusting strategies according to the specific risks and challenges of different altitudes, a more effective and efficient wildfire management system can be developed [49]. This approach provides a targeted response to the distinctive challenges presented by the proximity of urban areas to forest regions, contributing to a comprehensive strategy for fire management and prevention.

#### 4.5. Limitations

Despite the reliable performance of random convolution combined with machine learning in FFL estimation, this study has certain limitations that should be acknowledged. Firstly, FFL is a dynamic variable influenced by season and climate conditions. This study sampled FFL during the vegetation growth season and utilized synthetic Sentinel-2A imagery corresponding to that period. It is important to note that the spectral features captured by Sentinel-2A primarily reflect the overstory tree canopy conditions, which serve as indirect indicators of the understory surface fuels. These features, while not directly measuring the ground-level fuels, provide insights into the fuel accumulation patterns based on the overstory's light and volume scattering characteristics. Non-vegetation growth season FFL was not considered in this research. Secondly, another limitation of this study is the lack of predictions at smaller scales. Smaller prediction scales imply smaller image sizes, making it more challenging for random convolution to extract effective features from the images. Studies at smaller scales may require higher image resolution (this study used Sentinel-2A with a 10 m resolution). Another limitation of this study is the lack of utilization of imagery from other spatial scales, including both larger-scale imagery such as that from the Landsat series of satellites and smaller-scale imagery like QuickBird. While larger-scale imagery may lack detail, and smaller-scale imagery might contain more noise and shadows, the use of multi-scale imagery could enhance the potential of this technique, increasing the possibilities for predicting surface combustibles more accurately. Moreover, although the focus of this study is on surface combustibles, the extracted feature values can also be applied to estimate other related variables, such as canopy combustibles, forest biomass, and specifically vegetation conditions important to estimating fire behavior, including aboveground biomass, canopy bulk density, and base height. The spatial resolution of both Sentinel-2A imagery and the FFL maps in this study is relatively low, which may limit decision making at smaller spatial scales. Future research should consider using

higher-spatial-resolution imagery, such as Planetscope on the SuperDove platform with a 3 m pixel size and eight spectral bands [50], to create more precise FFL maps. This enhancement could enable more detailed decisions in mountain forest fire management, providing additional insights into the amount and distribution of FFL, especially important for cities and urban centers in managing fire prevention and mitigation.

## 5. Conclusions

This study employed Sentinel-2A imagery and leveraged the combination of random convolution and machine learning techniques to estimate FFL in the subtropical monsoon climate region of the study area, characterized by mixed broadleaf vegetation. The research involved extracting features from Sentinel-2A images of the study area using a random convolution algorithm. Various machine learning models, including RF, SVM, Lasso, and Ridge, were employed to establish FFL estimation models. This study found that smaller convolution kernel sizes were advantageous for constructing accurate FFL models. The optimal model was determined based on performance metrics, resulting in the creation of an FFL map for the study area. The results underscore the significant potential of employing Sentinel-2A imagery coupled with random convolution and machine learning as a viable alternative to extensive ground surveys for large-scale FFL estimation. The method of random convolution is adept at extracting a broader range of latent, quantifiable features from images. We believe that this approach can be instrumental in aiding other image-based analyses of different types of fuels or ecosystems. By leveraging the capabilities of random convolution, researchers can uncover intricate patterns and characteristics within ecological and fuel data that might not be evident through traditional analysis methods. This can lead to more comprehensive and accurate assessments in various ecological research and management applications. Concurrently, updated and reliable fuel maps should be utilized in conjunction with climatic data, topographic information, and details of important assets in the surrounding areas. Additionally, these fuel maps could serve as valuable data inputs for fire behavior models, providing crucial information for predicting and managing fire dynamics. This approach aids managers and decision-makers in formulating effective strategies for mountainous forest fire management and prevention, contributing to help target fuel mitigation activities. Given the proximity of urban areas to forests in the study region, regulating and guiding the behavior of residents might be a more effective strategy for fire prevention. Fire prevention strategies should place heightened emphasis on controlling human-made fire sources, particularly those related to ritual activities. This approach is crucial in areas where human activities interface closely with forested environments. However, it is important to acknowledge the limitations of this study. Future research should focus on enhancing the methods and approaches developed here, particularly in terms of utilizing additional remote sensing imagery for more accurate FFL prediction. Building on the findings of this study, further investigations could explore other dimensions and parameters that might influence FFL while staying within the scope of the current research.

**Author Contributions:** L.D. wrote the manuscript and designed the comparative experiments; D.M. supervised the study and revised the manuscript; E.Y. and J.J. revised the manuscript and gave comments and suggestions to the manuscript; J.J. assisted L.D. in designing the architecture and conducting experiments. All authors have read and agreed to the published version of the manuscript.

**Funding:** This research was funded by the Project of Technology Innovation Plan Project of Hunan Provincial Forestry and Grassland Department under Grant XLK202108-8 (Support: Dengkui Mo; Grant amount: 300,000 RMB), and in part by the National Natural Science Foundation of China under Grant 32071682 (Support: Dengkui Mo; Grant amount: 580,000 RMB) and Grant 31901311 (Support: Enping Yan; Grant amount: 250,000 RMB).

**Data Availability Statement:** Data are contained within the article.

**Conflicts of Interest:** The authors declare no conflict of interest.

## References

1. Moritz, M.A.; Batllori, E.; Bradstock, R.A.; Gill, A.M.; Handmer, J.; Hessburg, P.F.; Leonard, J.; McCaffrey, S.; Odion, D.C.; Schoennagel, T. Learning to coexist with wildfire. *Nature* **2014**, *515*, 58–66. [[CrossRef](#)] [[PubMed](#)]
2. Gale, M.G.; Cary, G.J.; Van Dijk, A.I.J.M.; Yebra, M. Forest fire fuel through the lens of remote sensing: Review of approaches, challenges and future directions in the remote sensing of biotic determinants of fire behaviour. *Remote Sens. Environ.* **2021**, *255*, 112282. [[CrossRef](#)]
3. Reich, R.M.; Lundquist, J.E.; Bravo, V.A. Spatial models for estimating fuel loads in the Black Hills, South Dakota, USA. *Int. J. Wildland Fire* **2004**, *13*, 119–129. [[CrossRef](#)]
4. Pollet, J.; Omi, P.N. Effect of thinning and prescribed burning on crown fire severity in ponderosa pine forests. *Int. J. Wildland Fire* **2002**, *11*, 1–10. [[CrossRef](#)]
5. Jenkins, M.E.; Bell, T.L.; Poon, L.F.; Aponte, C.; Adams, M.A. Production of pyrogenic carbon during planned fires in forests of East Gippsland, Victoria. *For. Ecol. Manag.* **2016**, *373*, 9–16. [[CrossRef](#)]
6. Stephens, S.L.; McIver, J.D.; Boerner, R.E.J.; Fettig, C.J.; Fontaine, J.B.; Hartsough, B.R.; Kennedy, P.L.; Schwilk, D.W. The Effects of Forest Fuel-Reduction Treatments in the United States. *BioScience* **2012**, *62*, 549–560. [[CrossRef](#)]
7. Plucinski, M.P. Contain and Control: Wildfire Suppression Effectiveness at Incidents and Across Landscapes. *Curr. For. Rep.* **2019**, *5*, 20–40. [[CrossRef](#)]
8. Raymond, C.L.; Peterson, D.L. Fuel treatments alter the effects of wildfire in a mixed-evergreen forest, Oregon, USA. *Can. J. For. Res.* **2005**, *35*, 2981–2995. [[CrossRef](#)]
9. Varner, J.M.; Kane, J.M.; Kreye, J.K.; Engber, E. The Flammability of Forest and Woodland Litter: A Synthesis. *Curr. For. Rep.* **2015**, *1*, 91–99. [[CrossRef](#)]
10. Prichard, S.J.; Kennedy, M.C.; Andreu, A.G.; Eagle, P.C.; French, N.H.; Billmire, M. Next-generation biomass mapping for regional emissions and carbon inventories: Incorporating uncertainty in wildland fuel characterization. *J. Geophys. Res. Biogeosci.* **2019**, *124*, 3699–3716. [[CrossRef](#)]
11. Loudermilk, E.L.; O'Brien, J.J.; Mitchell, R.J.; Cropper, W.P.; Hiers, J.K.; Grunwald, S.; Grego, J.; Fernandez-Diaz, J.C. Linking complex forest fuel structure and fire behaviour at fine scales. *Int. J. Wildland Fire* **2012**, *21*, 882–893. [[CrossRef](#)]
12. Brown, J.K. *Handbook for Inventorying Downed Woody Material*; USDA: Ogden, UT, USA, 1974.
13. Picard, N.; Henry, M.; Mortier, F.; Trotta, C.; Saint-André, L. Using Bayesian Model Averaging to Predict Tree Aboveground Biomass in Tropical Moist Forests. *For. Sci.* **2012**, *58*, 15–23. [[CrossRef](#)]
14. Rentería-Anima, J.B.; Treviño-Garza, E.; Nívar-Chaidez, J.d.J.; Aguirre-Calderón, O.; Cantú-Silva, I. Caracterización de combustibles leñosos en el ejido Pueblo Nuevo, Durango. *Rev. Chapingo Ser. Cienc. For. Ambiente* **2005**, *11*, 51–56.
15. Güngöroglu, C.; Güney, Ç.O.; Sari, A.; Serttaş, A. Predicting crown fuel biomass of Turkish red pine (*Pinus brutia* Ten.) for the Mediterranean regions of Turkey. *Šumarski List* **2018**, *142*, 601–610. [[CrossRef](#)]
16. Wells, A.G.; Munson, S.M.; Sesnie, S.E.; Villarreal, M.L. Remotely Sensed Fine-Fuel Changes from Wildfire and Prescribed Fire in a Semi-Arid Grassland. *Fire* **2021**, *4*, 84. [[CrossRef](#)]
17. Fensham, R.J. The management implications of fine fuel dynamics in Bushlands Surrounding Hobart, Tasmania. *J. Environ. Manag.* **1992**, *36*, 301–320. [[CrossRef](#)]
18. Arroyo, L.A.; Pascual, C.; Manzanera, J.A. Fire models and methods to map fuel types: The role of remote sensing. *For. Ecol. Manag.* **2008**, *256*, 1239–1252. [[CrossRef](#)]
19. Saatchi, S.; Halligan, K.; Despain, D.G.; Crabtree, R.L. Estimation of forest fuel load from radar remote sensing. *IEEE Trans. Geosci. Remote Sens.* **2007**, *45*, 1726–1740. [[CrossRef](#)]
20. Andersen, H.-E.; McGaughey, R.J.; Reutebuch, S.E. Estimating forest canopy fuel parameters using LIDAR data. *Remote Sens. Environ.* **2005**, *94*, 441–449. [[CrossRef](#)]
21. Chen, Y.; Zhu, X.; Yebra, M.; Harris, S.; Tapper, N. Development of a predictive model for estimating forest surface fuel load in Australian eucalypt forests with LiDAR data. *Environ. Model. Softw.* **2017**, *97*, 61–71. [[CrossRef](#)]
22. Rolf, E.; Proctor, J.; Carleton, T.; Bolliger, I.; Shankar, V.; Ishihara, M.; Recht, B.; Hsiang, S. A generalizable and accessible approach to machine learning with global satellite imagery. *Nat. Commun.* **2021**, *12*, 4392. [[CrossRef](#)] [[PubMed](#)]
23. Ensley-Field, M.; Shriver, R.K.; Law, S.; Adler, P.B. Combining Field Observations and Remote Sensing to Forecast Fine Fuel Loads. *Rangel. Ecol. Manag.* **2023**, *90*, 245–255. [[CrossRef](#)]
24. Nolan, R.H.; Price, O.F.; Samson, S.A.; Jenkins, M.E.; Rahmani, S.; Boer, M.M. Framework for assessing live fine fuel loads and biomass consumption during fire. *For. Ecol. Manag.* **2022**, *504*, 119830. [[CrossRef](#)]
25. Jin, S.; Chen, S.-C. Application of QuickBird imagery in fuel load estimation in the Daxinganling region, China. *Int. J. Wildland Fire* **2012**, *21*, 583–590. [[CrossRef](#)]
26. Brandis, K.; Jacobson, C. Estimation of vegetative fuel loads using Landsat TM imagery in New South Wales, Australia. *Int. J. Wildland Fire* **2003**, *12*, 185–194. [[CrossRef](#)]
27. Franke, J.; Barradas, A.C.S.; Borges, M.A.; Menezes Costa, M.; Dias, P.A.; Hoffmann, A.A.; Orozco Filho, J.C.; Melchiori, A.E.; Siegert, F. Fuel load mapping in the Brazilian Cerrado in support of integrated fire management. *Remote Sens. Environ.* **2018**, *217*, 221–232. [[CrossRef](#)]
28. D'Este, M.; Elia, M.; Giannico, V.; Spano, G.; Laforteza, R.; Sanesi, G. Machine Learning Techniques for Fine Dead Fuel Load Estimation Using Multi-Source Remote Sensing Data. *Remote Sens.* **2021**, *13*, 1658. [[CrossRef](#)]

29. Li, Z.; Angerer, J.P.; Jaime, X.; Yang, C.; Wu, X.B. Estimating rangeland fine fuel biomass in Western Texas using high-resolution aerial imagery and machine learning. *Remote Sens.* **2022**, *14*, 4360. [[CrossRef](#)]
30. City Local Chronicles Compilation Office. Overview of Changsha. Available online: [http://www.changsha.gov.cn/xfzs/zjmlzs/zsagl/200907/t20090727\\_5686409.html](http://www.changsha.gov.cn/xfzs/zjmlzs/zsagl/200907/t20090727_5686409.html) (accessed on 15 November 2023).
31. Liu, Y.; Xiong, J.; Zhang, L. Study on Spatio-Temporal Distribution Characteristics of Forest Fire in Hunan Province. *Cent. S. For. Inventory Plan.* **2021**, *40*, 17–21. [[CrossRef](#)]
32. Hu, T.; Ma, L.; Gao, Y.; Fan, J.; Sun, L. Modification and Comparison of Methods for Predicting the Moisture Content of Dead Fuel on the Surface of *Quercus mongolica* and *Pinus sylvestris* var. *mongolica* under Rainfall Conditions. *Fire* **2023**, *6*, 379. [[CrossRef](#)]
33. Drusch, M.; Del Bello, U.; Carlier, S.; Colin, O.; Fernandez, V.; Gascon, F.; Hoersch, B.; Isola, C.; Laberinti, P.; Martimort, P. Sentinel-2: ESA's optical high-resolution mission for GMES operational services. *Remote Sens. Environ.* **2012**, *120*, 25–36. [[CrossRef](#)]
34. Mutanga, O.; Kumar, L. Google earth engine applications. *Remote Sens.* **2019**, *11*, 591. [[CrossRef](#)]
35. Romero, A.; Gatta, C.; Camps-Valls, G. Unsupervised deep feature extraction for remote sensing image classification. *IEEE Trans. Geosci. Remote Sens.* **2015**, *54*, 1349–1362. [[CrossRef](#)]
36. Jain, P.; Coogan, S.C.P.; Subramanian, S.G.; Crowley, M.; Taylor, S.; Flannigan, M.D. A review of machine learning applications in wildfire science and management. *Environ. Rev.* **2020**, *28*, 478–505. [[CrossRef](#)]
37. Labenski, P.; Ewald, M.; Schmidlein, S.; Heinsch, F.A.; Fassnacht, F.E. Quantifying surface fuels for fire modelling in temperate forests using airborne lidar and Sentinel-2: Potential and limitations. *Remote Sens. Environ.* **2023**, *295*, 113711. [[CrossRef](#)]
38. Arellano-Pérez, S.; Castedo-Dorado, F.; López-Sánchez, C.A.; González-Ferreiro, E.; Yang, Z.; Díaz-Varela, R.A.; Álvarez-González, J.G.; Vega, J.A.; Ruiz-González, A.D. Potential of Sentinel-2A Data to Model Surface and Canopy Fuel Characteristics in Relation to Crown Fire Hazard. *Remote Sens.* **2018**, *10*, 1645. [[CrossRef](#)]
39. Jazebi, S.; De Leon, F.; Nelson, A. Review of wildfire management techniques—Part I: Causes, prevention, detection, suppression, and data analytics. *IEEE Trans. Power Deliv.* **2019**, *35*, 430–439. [[CrossRef](#)]
40. Miller, R.K.; Field, C.B.; Mach, K.J. Barriers and enablers for prescribed burns for wildfire management in California. *Nat. Sustain.* **2020**, *3*, 101–109. [[CrossRef](#)]
41. Moreira, F.; Ascoli, D.; Safford, H.; Adams, M.A.; Moreno, J.M.; Pereira, J.M.; Catry, F.X.; Armesto, J.; Bond, W.; González, M.E. Wildfire management in Mediterranean-type regions: Paradigm change needed. *Environ. Res. Lett.* **2020**, *15*, 011001. [[CrossRef](#)]
42. Anderson, W.R.; Catchpole, E.; Butler, B. Convective heat transfer in fire spread through fine fuel beds. *Int. J. Wildland Fire* **2010**, *19*, 284–298. [[CrossRef](#)]
43. Gould, J.S.; McCaw, W.L.; Cheney, N.P. Quantifying fine fuel dynamics and structure in dry eucalypt forest (*Eucalyptus marginata*) in Western Australia for fire management. *For. Ecol. Manag.* **2011**, *262*, 531–546. [[CrossRef](#)]
44. Lasaponara, R.; Lanorte, A. Remotely sensed characterization of forest fuel types by using satellite ASTER data. *Int. J. Appl. Earth Obs. Geoinf.* **2007**, *9*, 225–234. [[CrossRef](#)]
45. Hudak, A.T.; Bright, B.C.; Pokswinski, S.M.; Loudermilk, E.L.; O'Brien, J.J.; Hornsby, B.S.; Klauberg, C.; Silva, C.A. Mapping forest structure and composition from low-density LiDAR for informed forest, fuel, and fire management at Eglin Air Force Base, Florida, USA. *Can. J. Remote Sens.* **2016**, *42*, 411–427. [[CrossRef](#)]
46. Duff, T.J.; Bell, T.L.; York, A. Predicting continuous variation in forest fuel load using biophysical models: A case study in south-eastern Australia. *Int. J. Wildland Fire* **2012**, *22*, 318–332. [[CrossRef](#)]
47. Hanes, C.C.; Wotton, M.; Woolford, D.G.; Martell, D.L.; Flannigan, M. Mapping organic layer thickness and fuel load of the boreal forest in Alberta, Canada. *Geoderma* **2022**, *417*, 115827. [[CrossRef](#)]
48. Rigolot, E. Fuel-break assessment with an expert appraisal approach. In *Forest Fire Research and Wildland Fire Safety, Proceedings of the IV International Conference on Forest Fire Research 2002 Wildland Fire Safety Summit, Coimbra, Portugal, 18–23 November 2002*; Millpress Science Publishers: Amsterdam, The Netherlands, 2002.
49. Agee, J.K.; Skinner, C.N. Basic principles of forest fuel reduction treatments. *For. Ecol. Manag.* **2005**, *211*, 83–96. [[CrossRef](#)]
50. Roy, D.P.; Huang, H.; Houborg, R.; Martins, V.S. A global analysis of the temporal availability of PlanetScope high spatial resolution multi-spectral imagery. *Remote Sens. Environ.* **2021**, *264*, 112586. [[CrossRef](#)]

**Disclaimer/Publisher's Note:** The statements, opinions and data contained in all publications are solely those of the individual author(s) and contributor(s) and not of MDPI and/or the editor(s). MDPI and/or the editor(s) disclaim responsibility for any injury to people or property resulting from any ideas, methods, instructions or products referred to in the content.